

# Design of an L-band normally conducting RF gun cavity for high peak and average RF power



V. Paramonov<sup>a,\*</sup>, S. Philipp<sup>b</sup>, I. Rybakov<sup>a</sup>, A. Skassyrskaya<sup>a</sup>, F. Stephan<sup>b</sup>

<sup>a</sup> Institute for Nuclear Research of Russian Academy of Sciences, 60-th October Anniversary prospect 7a, 117312 Moscow, Russia

<sup>b</sup> Deutsches Elektronen-Synchrotron DESY, Platanenallee 6, D-15738 Zeuthen, Germany

## ARTICLE INFO

### PACS:

29.00.-c

29.25.Bx

07.05.Tp

41.60.Cr

### Keywords:

Free electron laser

RF gun

Pulsed RF heating

Average RF power

## ABSTRACT

To provide high quality electron bunches for linear accelerators used in free electron lasers and particle colliders, RF gun cavities operate with extreme electric fields, resulting in a high pulsed RF power. The main L-band superconducting linacs of such facilities also require a long RF pulse length, resulting in a high average dissipated RF power in the gun cavity. The newly developed cavity based on the proven advantages of the existing DESY RF gun cavities, underwent significant changes. The shape of the cells is optimized to reduce the maximal surface electric field and RF loss power. Furthermore, the cavity is equipped with an RF probe to measure the field amplitude and phase. The elaborated cooling circuit design results in a lower temperature rise on the cavity RF surface and permits higher dissipated RF power. The paper presents the main solutions and results of the cavity design.

## 1. Introduction

To provide high quality electron bunches with a high peak current as well as exceptionally small transverse emittance for free electron lasers, such as the European XFEL [1] and FLASH [2], the L-band RF gun cavities should operate with an extreme electric field on the photo cathode  $E_c \sim 60$  MV/m, resulting in a high pulsed RF power, up to  $P_t \sim 6.5$  MW in the cavity. The main L-band linacs in these facilities are realized with superconducting RF technology and operate in a long,  $\sim 1$  ms, RF pulse mode. This directly defines the long pulse operation mode for the RF gun cavity as  $\tau \sim (650 \div 1000)$   $\mu$ s. Together with a repetition rate of 10 Hz or more, it defines a very high average RF power of more than 50 kW, dissipated in a rather short cavity of  $\sim 25$  cm length.

Similar parameters for the electron beam and the main linac define similar parameters for RF gun operation in colliders like ILC which is also based on a superconducting L-band linac [3].

For a reliable cavity operation the temperature rise at the cavity RF surface should be as small as possible. Furthermore, the temperature gradient over the whole cavity should be small in order to keep the internal thermal stress within the elastic limit of the cavity material.

To allow a high performance of the generated electron bunches the distribution of the electromagnetic field should be without higher order modes additions caused by deterioration of the azimuthal cavity symmetry.

For L-band cavities electric and magnetic field values on the surface are lower compared to S-band or X-band accelerating structures operating with a high accelerating gradient but short RF pulses. For L-band RF gun operation with the peak electric field at the cathode of  $E_c = 60 \frac{\text{MV}}{\text{m}}$  the peak pulsed RF loss density reaches  $P_d \approx 4.8 \times 10^7 \frac{\text{W}}{\text{m}^2}$  and significant pulsed RF heating effects take place due to the RF pulse length. When exceeding safe values for the surface temperature rise and stress, this effect restricts possible combinations of electric field on the cathode  $E_c$  and RF pulse length  $\tau$  for reliable operation.

During a long RF pulse the own frequency of the gun cavity changes by quite detectable values, see [4] for example. However, the phase of the RF oscillations in the gun cavity should be controlled, hence detected, with a maximal possible precision for correct synchronization with the main linac RF system to provide the required beam quality. The RF phase in the gun cavity can be estimated with different methods, but the most precise and reliable one is a direct phase measurement with a RF probe in the cavity cell. The implementation of a RF probe in the cavity design generates a set of coupled problems, which should not deteriorate other cavity operational performances.

In the development of DESY L-band RF gun cavities, starting with [5], several modifications with consistent improvements were developed and tested in operation. To distinguish essential changes, these modifications are referred to as gun 2, gun 3 and gun 4. The last two options, gun 3 and gun 4, are shown in Fig. 1 to illustrate the difference in their design. These options have the same cavity cell shape and

\* Corresponding author.

E-mail address: [paramono@inr.ru](mailto:paramono@inr.ru) (V. Paramonov).

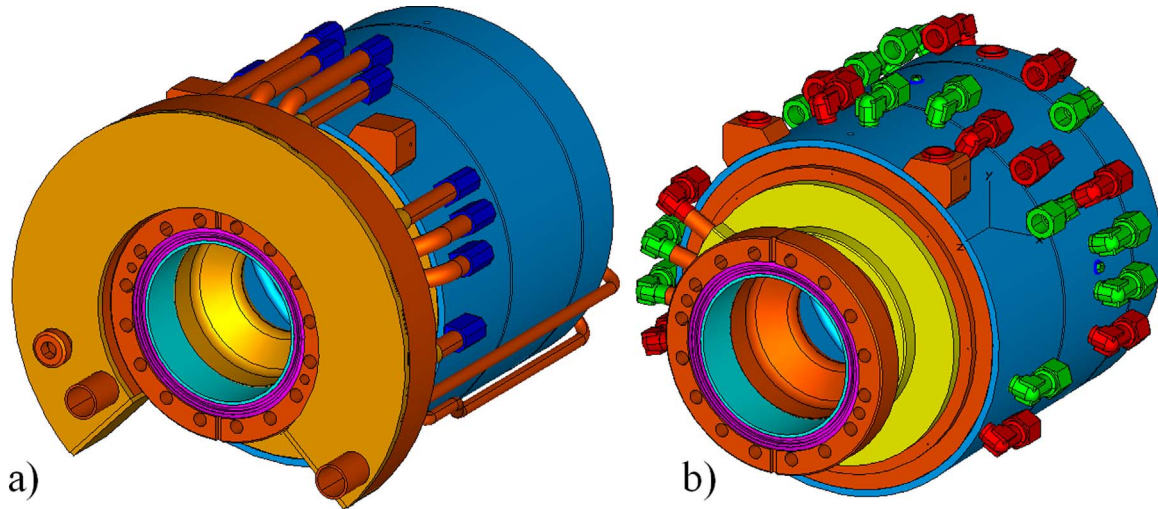


Fig. 1. The models of existing DESY gun cavities, gun 3 (a) and gun 4 (b).

coaxial RF coupler [5]. The main difference between gun 3 and gun 4 [6] is in the improvement of the cooling circuit.

During the operation of the DESY L-band RF gun cavities, desires for further improvements were formulated. The next step in the gun cavity development, named gun 5, is based on the proven advantages of the existing cavities but includes significant improvements. The main attention was paid to mutual optimizations of coupled processes in the cavity, operating in combination of a high electric field on the cathode,  $E_c = 60 \frac{MV}{m}$ , long RF pulse  $\sim 1$  ms, high RF pulse power and average dissipated RF power. The main improvements over the previous gun cavity generation are:

- the improved cell and iris shapes,
- the RF pick up in the full cavity cell,
- the improved water cooling.

All simulations for the cavity development were performed by using the software ANSYS [7] and CST MWS [8].

## 2. General cavity design

The developed cavity design is shown in Fig. 2. Similar to the existing cavities, the cavity body consists of three

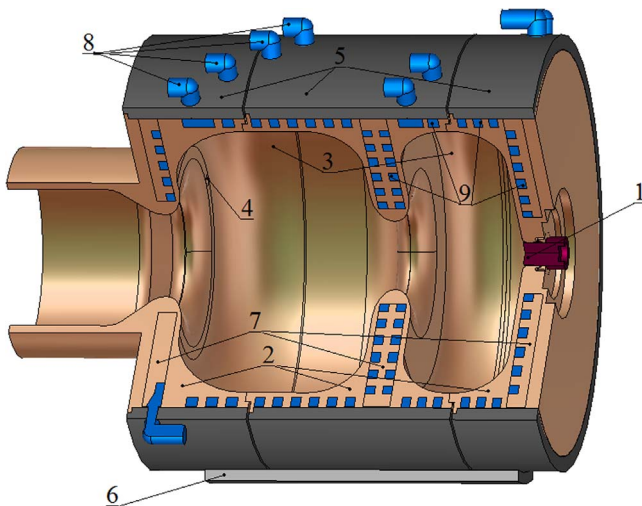


Fig. 2. The developed gun 5 cavity design. 1 – cathode, 2 – three copper parts of the cavity body, 3 – cavity cells, 4 – RF probe position, 5 – jackets, 6 – stiffening rib, 7 – disks with cooling channels, 8 – water input/output, 9 – cooling channels.

parts made of OFHC copper. In the existing cavities for cooling the iris between the first and the second cells there is a recess from outside, where a disk with cooling channels is located. In gun 5 this idea is applied to all three walls with radial cooling channels before, between and after the cavity cells.

Furthermore, in the existing cavities the copper parts are covered with stainless steel jackets. These jackets provide a stable hold for placing the input/output water connectors, temperature sensors and accessories for cavity mounting and adjustment. In the design for gun 5 jackets are joined together with three stiffening ribs, [9], manufactured from the same stainless steel and placed with  $120^\circ$  separations in azimuthal direction. These ribs improve the cavity rigidity, protect the brazed surfaces between the copper parts and restrict the cavity deformations, caused by pulsed RF heating during the RF pulse.

The assemblage of all cavity parts into one solid body is made by multi – step high temperature brazing. As well as all the previous cavities, gun 5 has no brazed water-vacuum joints. This technology is well proven in the existing DESY gun cavities.

Properties of the materials for different cavity parts are listed in Table 1. The most important are properties of annealed OFHC copper, which differ in some range in various references, thus providing deviations in the results of simulations. In our consideration we use parameters for fully annealed OFHC, presented in [10]. The parameters of the developed cavity are considered for the operating regime with  $E_c = 60 \frac{MV}{m}$ ,  $\tau = 1$  ms and a 10 Hz pulse repetition rate.

Table 1  
Material properties used for simulations of coupled effects.

Parameter	Units	OFHC,annealed, [10]	Steel AISI 316	Molybdenum
Density, $\rho$	$\frac{kg}{m^3}$	8950	8000	10200
Specific heat, $C_p$	$\frac{J}{kg K}$	385	460	256
Heat conductivity, $k_c$	$\frac{W}{m K}$	391	16.3	14.2
Thermal expansion, $\alpha$	$\frac{1}{K}$	$1.67 \times 10^{-5}$	$1.59 \times 10^{-5}$	$4.9 \times 10^{-6}$
Elastic modulus, $E_{Ym}$	GPa	123	193	336.3
Poisson's ratio, $\nu$		0.345	0.28	0.3
Yield stress, $\sigma_Y$	MPa	62		
Electric conductivity, $\sigma$	$\frac{S}{m}$	$5.8 \times 10^7$		$1.73 \times 10^7$

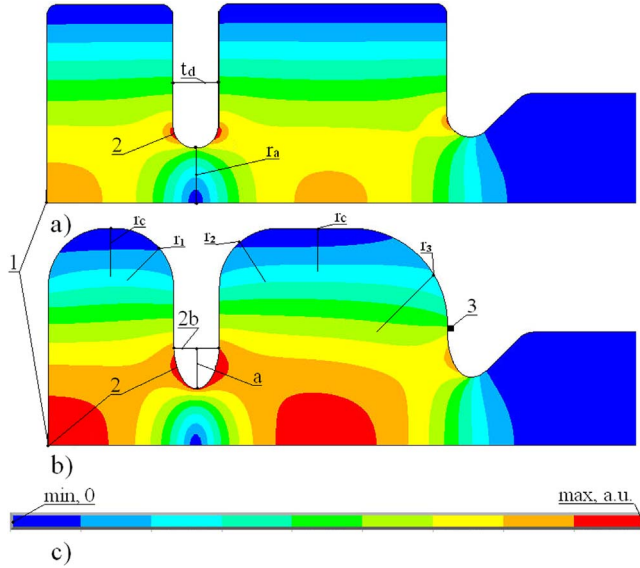


**Fig. 3.** The maps of electric field intensity in the cross sections of the existing DESY gun cavities, (a), and gun 5, (b). (c) is the color scale for field intensity in arbitrary units, 1 – position of the photo cathode, 2 – position of  $E_{s \max}$ , 3 – RF probe position.

### 3. RF parameters

The shape of the cavity cells was reconsidered and optimized to reduce the maximum value of the electric field  $E_{s \max}$  on the cavity surface as well as the pulse RF power  $P_i$  required for the given electric field on the cathode  $E_c$ .

Different shapes for cavity cells were considered [11] and analyzed in connection with beam dynamics simulations and other cavity parameters. No reasonable arguments were found to change the iris thickness  $t_d$  and iris aperture  $r_a$ , see Fig. 3a, and cells length as compared to the reference cells design [5]. But an elliptical shape of the iris tip is intended to reduce  $E_{s \max}$  in the cavity. The minimal accessible  $E_{s \max}$  depends on the  $\frac{d}{r_a}$  ratio as well as on the  $\frac{a}{b}$  ratio of the ellipse axes, Fig. 3b. The last ratio was optimized to reduce  $E_{s \max}$ , which now occurs on the iris tip from the side of the full cavity cell but the electric field on the cathode is almost as high as  $E_{s \max} \approx E_c$ . In Fig. 3 color maps of the electric field intensity  $|E|$  are shown for the reference cavity, [5], at the top, and the developed cavity, at the bottom. As one can see, for gun 5 a stronger electric field is expected around the photo cathode.

The application of an elliptical iris tip results in a small increase of the required RF power. To decrease the required  $P_i$ , cell roundings in the outer parts are applied. To better suit the cooling circuit both cells have the same outer radius  $r_c$ . Combinations of cells radius  $r_c$  and radii of cells rounding  $r_1, r_2, r_3$  are used to fit the operating frequency, to gain space for placing an RF probe at the flat part of the front wall and to balance the field in the cavity cells.

The new cavity has a higher own quality factor  $Q_0$  and a lower required  $P_i$  value. Also the elliptical iris tip results in an increase of coupling between the cavity cells and the frequency separation between the operating  $\pi$ -type mode  $f_\pi$  and the 0-type mode  $f_0$  increases, improving the stability of the cavity parameters.

The beam dynamics simulations [11] with the ASTRA code [12] showed that the changes in the cells shape and the corresponding field distributions do not significantly change the electron bunch dynamics.

The cavity is intended for applications with the same coaxial RF coupler as the existing gun cavities. Due to a higher quality factor the calculated insertion of the RF coupler should be 1.7 mm less than that in the reference cavity [5].

The possibility of multipactoring was studied for the developed cavity in comparison with the reference cavity according to the

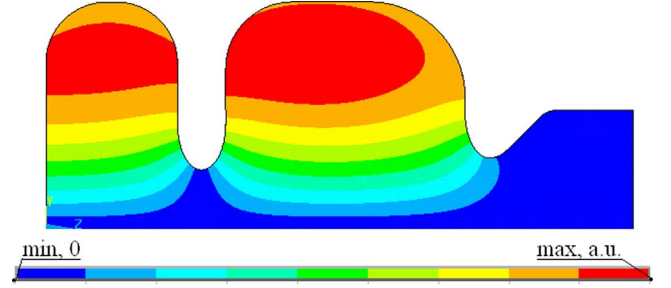


**Fig. 4.** The map of magnetic field intensity in the cross section of gun 5 and the color scale for field intensity, a.u.

procedure given in [13]. No conditions for a stable electron cloud were found near the cavity operating regime. For the same assumption on the Secondary Electron Yield (SEY) for annealed OFHC copper, [14], simulations show even a faster decreasing in the number of secondary electrons as compared to the reference cavity geometry. This is quite understandable since the cell shape for the designed cavity is more similar to the TESLA cells shape, which was developed to suppress the emission of secondary electrons.

The value of the maximal magnetic field on the cavity surface  $H_{s \max}$  defines the RF loss density, both for pulsed and average cavity RF heating. This value also should be as small as possible. For RF gun cavities we can connect  $E_c$  and  $H_{s \max}$  values by the relation:

$$Z_h = \frac{E_c}{H_{s \max}}, \text{ [Ohm]}, \quad (1)$$

where  $Z_h$  is a parameter of the cavity geometry. For gun cavities the electric field on the photo cathode  $E_c$  is defined by the requirements of the bunch dynamics and the only way to reduce  $H_{s \max}$  is to optimize the cavity shape for a higher  $Z_h$ . A color map of the magnetic field intensity  $|H|$  for gun 5 is shown in Fig. 4.

For gun 5 the parameter  $Z_h$  is practically the same as for the reference cavities,  $\approx 575$  Ohm and  $\approx 590$  Ohm, respectively. For cavities operating in the  $TM_{011}$  mode we cannot improve  $Z_h$  without deteriorating the cooling conditions and the mechanical strength.

### 4. RF probe implementation

The RF probe is developed with strict requirements such as minimizing the perturbation of the field distribution and keeping a low pulsed heating. Furthermore, the probe should be matched to the cavity, have a high mechanical reliability and low impact on the cavity cooling. The whole setup must be also compatible to the photo injector installation.

Facing these requirements, we studied all the effects connected to the RF probe in special simulations with an equivalent sector type cavity. It was reduced in longitudinal direction to have the most possible mesh density and precision of results. Details of the RF probe hole in the model for the equivalent sector type cavity in  $TM_{010}$  mode are shown in Fig. 5a, where  $r_h$  is the radius of the probe hole and  $r_b$  is the radius of rounding for hole edge.

#### 4.1. Local fields enhancement in RF probe vicinity

The distortions in the cavity surface in the vicinity of the RF probe are always accompanied by the distortions in the electromagnetic field, as shown in Fig. 5b,c. Since maximum values are of interest, we will describe the field distortions with parameters of field enhancement,  $\frac{H_{h \max}}{H_{h0}}, \frac{E_{h \max}}{E_{h0}}$ , where  $H_{h \max}, E_{h \max}$  are the maximal values of magnetic and electric field intensities in the probe vicinity and  $H_{h0}, E_{h0}$  are the values of field intensities at the point of the probe hole in case of an unperturbed cavity.

For the hole dimensions  $r_h$  and  $r_b$  (see Fig. 5a) much smaller than a

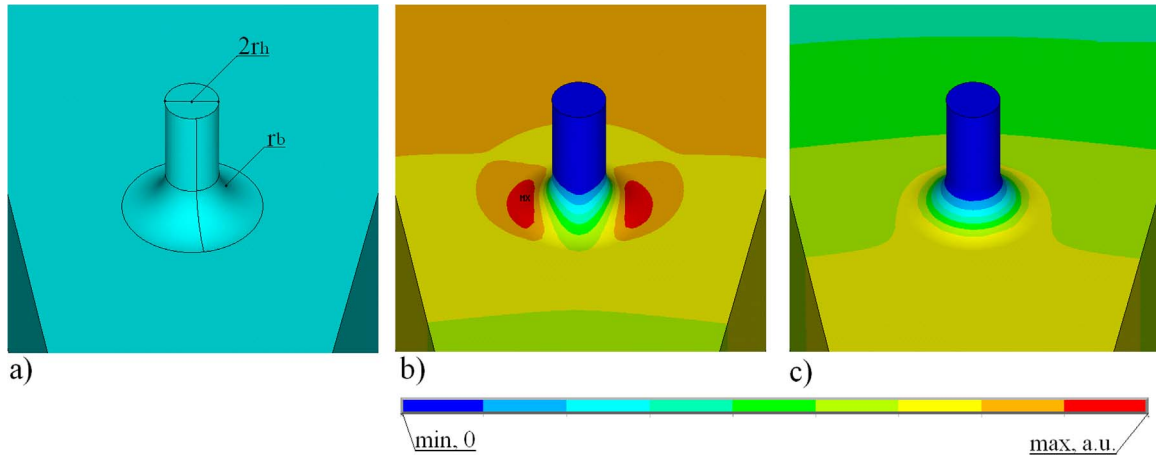


Fig. 5. The part of the equivalent cavity in the vicinity of the RF probe hole, (a) and distributions of magnetic (b) and electric (c) field intensities in the vicinity of the hole,  $\frac{r_b}{r_h} = 1.6$ , external view.

quarter of the operating wavelength  $\lambda$ , the field distributions in the nearest hole vicinity depend only on the ratio  $\frac{r_b}{r_h}$ . In this case it does not depend on the absolute values of  $r_h$  and  $r_b$  which is a consequence of static field approximation around the hole. The results of numerical simulations confirm this statement for the explored region in the range  $r_h = (1 \text{ mm} \div 2.6 \text{ mm})$  and  $r_b = (0.125 \div 4)r_h$ .

The hole generates different perturbations in the distributions of electric and magnetic fields. The perturbation is dipole like for the magnetic field, Fig. 5b and monopole like for the electric field, Fig. 5c.

The calculated values for enhancement of the magnetic and the electric fields are plotted in Fig. 6a. For the same  $\frac{r_b}{r_h}$  ratio the enhancement of the magnetic field is larger than that of the electric field and their relation can be roughly approximated as  $\frac{H_{max}}{H_0} \approx (\frac{E_{max}}{E_0})^2$ . With  $\frac{r_b}{r_h}$  increasing above  $\frac{r_b}{r_h} \approx 1$  the field enhancement saturates and the further enlargement of the radius for the rounding of the hole edge  $r_b$  has a small effect.

The local enhancement of the magnetic field leads to a stronger enhancement of the RF loss density, Fig. 6b, which is essential for pulsed RF heating. The implementation of a RF probe should not deteriorate other cavity performances and after an RF pulse the temperature rise  $T_{sp}$  in the probe vicinity should not exceed the maximal temperature rise of another cavity surface. From plotting  $(\frac{H_{max}}{H_0})^2$  in Fig. 6b one can conclude that practically there is no RF loss density enhancement lower than 1.5 and realistic values in the range of  $1.6 \leq (\frac{H_{max}}{H_0})^2 \leq 2.0$  can be obtained for  $1 \leq \frac{r_b}{r_h} \leq 3$ . The distribution of the pulsed RF loss density  $P_d$  on the cavity surface is shown in Fig. 7

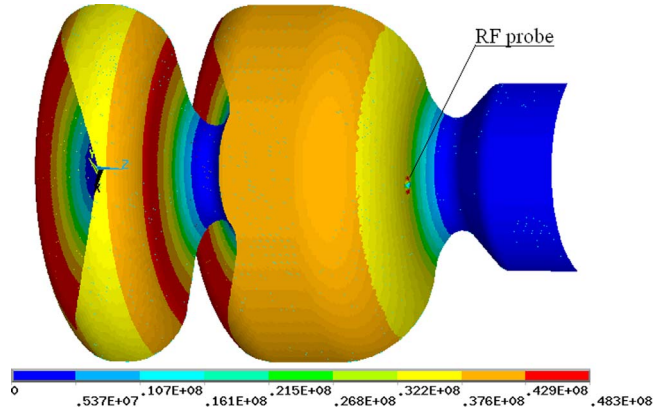


Fig. 7. The distribution of the pulsed RF loss density  $P_d$ , in  $\frac{W}{m^2}$ , on the cavity surface.

for the sector of 120 degrees. Analyzing the distribution of the RF loss density on the cavity surface, Fig. 7, we see that allocation of the RF probe on the outer surface of the cavity is unfavorable. Even with the minimal enhancement  $\frac{H_{max}^2}{H_0^2} = 1.5$ , the probe vicinity would show the highest RF loss density of the whole cavity surface, resulting in the highest temperature rise after the RF pulse. Therefore, the RF probe should be moved to the regions with lower density of RF losses - either to the cathode wall or to the front cavity wall. The RF probe on the cathode wall is not compatible with other equipment of the photo

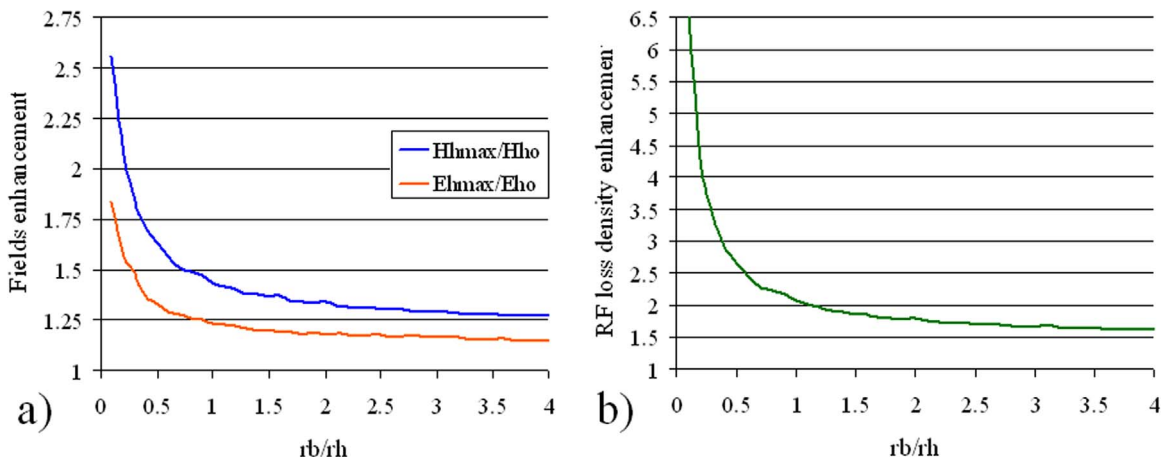


Fig. 6. The plots for enhancement of magnetic  $\frac{H_{max}}{H_0}$  and electric  $\frac{E_{max}}{E_0}$  fields (a) and the plot of RF loss density enhancement  $\frac{H_{max}^2}{H_0^2}$ , (b), in the probe hole vicinity,  $r_h = (1 \text{ mm} \div 2.6 \text{ mm})$ .

injector, namely the backing solenoid. So there is only one possibility to place the RF probe on the front cavity wall.

Due to a lower enhancement of the electric field  $(\frac{E_{max}}{E_0})^2 \leq 1.25$ , Fig. 6a, we can select on the front cavity wall an appropriate probe position, see Fig. 3, to have the resulting electric field in the probe vicinity less than the maximal electric field on the other part of the cavity surface.

#### 4.2. Perturbation of field distribution in the cavity

Together with a local perturbation of the field distribution in the vicinity, the hole for the RF probe will generate a field perturbation in the total cavity. According to the generalized perturbation theorem, [18], the field  $\vec{E}$  in a slightly deformed cavity with the volume  $V = V_0 + \Delta V$  can be described as:

$$\vec{E} \approx \vec{E}_n + \sum_{m \neq n} \vec{E}_m \frac{\omega_m^2 \int_{\Delta V} (Z_0^2 \vec{H}_m \vec{H}_n^* - \vec{E}_m \vec{E}_n^*) dV}{W_0(\omega_n^2 - \omega_m^2)}, \quad Z_0 = \sqrt{\frac{\mu_0}{\epsilon_0}}, \quad (2)$$

where  $V_0$  is the volume,  $\omega_m$ ,  $\vec{E}_m$ ,  $\vec{H}_m$  are the own frequencies and fields of the modes in the unperturbed cavity,  $W_0$  is the stored energy of the fields,  $\Delta V$  is the volume of perturbation,  $\epsilon_0$  and  $\mu_0$  are the permittivity and permeability of vacuum, respectively, and the sum is over all possible modes,

For the RF gun cavity the operating mode with symbol  $n$  in Eq. (2) is  $TM_{011}$ . Below the cut off frequency of the RF coupler in the cavity spectrum there are three dipole High Order Modes (HOMs) and only one quadrupole HOM with the frequency of  $\approx 2100$  MHz.

For RF measurements only one RF probe is sufficient. The single hole couples with the operating mode of all HOMs with azimuthal field dependence. With two symmetrically placed holes in Eq. (2) for dipole HOMs the coupling integral over the first hole cancels the integral over the second hole and the additions in the field from dipole modes disappear. To simplify cavity design, the second symmetrical hole is realized as imitation, without RF probe, with the same radius of rounding  $r_b$  but with the decreased length of the cylindrical part. With two symmetrical holes the contribution of quadrupole modes doubles. The way to reduce the contribution of quadrupole modes is to decrease the value of the coupling integral in Eq. (2).

The hole dimensions are much less as compared to a typical distance of field variation for all cavity modes and we can rewrite Eq. (2) for this quadrupole HOM as:

$$\vec{E} \approx \vec{E}_0 + \frac{\omega_q^2 (Z_0^2 \vec{H}_{qh} \vec{H}_{0h} n^* - \vec{E}_{qh} \vec{E}_{0h}^*) \Delta V \vec{E}_q}{W_0(\omega_0^2 - \omega_q^2)} \quad (3)$$

where  $\vec{H}_{qh}$  and  $\vec{E}_{qh}$  are the HOM fields at the RF probe hole position. The additions in the field distribution are proportional to the volume of perturbation  $\Delta V$  which rises fast,  $\Delta V \sim r_h^3$  for  $\frac{r_b}{r_h} = const$  and  $\Delta V \sim r_b^2$  for  $r_h = const$ , with the increase of the absolute probe hole dimensions.

From requirements of mechanical treatment we cannot select very small values for  $r_h$  and  $\frac{r_b}{r_h}$  but, to reduce field perturbation in the cavity, we should keep them as small as possible. As a compromise,  $r_h = 1.25$  mm,  $r_b = 2$  mm were chosen.

For numerical estimations, simulations with special care for precision of the field calculation were performed with the cavity model, shown in Fig. 8. Three rings,  $n1$ ,  $n2$ ,  $n3$  with a radius of 10 mm were introduced for fields estimation. They were placed at a distance of 12.5 mm from the cathode in the half cell,  $n1$ , from the iris plane in the full cell,  $n2$  and from the front wall in the full cell,  $n3$ .

In simulations for the cavity with RF probes, at the background of the own numerical noises we cannot distinguish any regular deviations in the field components along the circles  $n1$ ,  $n2$  and  $n3$ . Only by subtracting the own noises from simulations of the cavity without probes we can see regular field perturbations by the ‘relative deviation’

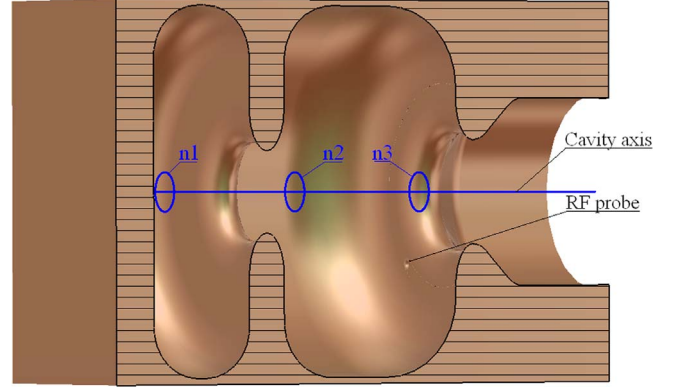


Fig. 8. The model for estimation of the field perturbation by two symmetrically placed RF probes.

$-RD_j$ , which is calculated by:

$$RD_j = \frac{E_j^r - E_{jav}^r}{E_{jav}^r} - \frac{E_j^h - E_{jav}^h}{E_{jav}^h}, \quad (4)$$

where  $E_j$  is the  $E_z, E_r$  or  $H_\phi$  field component and  $E_{jav}$  is the average value of the  $E_j$  component along the circle. Here the superscripts  $h$  and  $r$  indicate the calculated values for the cavity with and without RF probe, respectively. In the cathode cells, which is the most critical for bunch formation, along circle  $n1$ , even with filtering of own numerical noises, we can not distinguish regular field perturbations with a relative level above  $3.0 \times 10^{-7}$  for each field component. In the full cell near the iris we clearly see quadrupole addition in  $E_r, H_\phi$  field components along the circle  $n2$  with relative values  $\leq 5.0 \times 10^{-5}$ , Fig. 9a. The strongest quadrupole addition takes place near the cavity exit along the circle  $n3$  (see Fig. 9b) with relative values for  $E_r \leq 1.3 \times 10^{-4}$  and  $H_\phi \leq 2.0 \times 10^{-5}$ . The results of treatment show that the detected quadrupole addition in the field distribution is far below the current resolution limits for typical simulations and measurements of field distributions and simulations of bunch dynamics. Moreover, the results confirm a theoretical prediction from Eqs. (2) showing coupling with the HOM quadrupole  $TE_{211}$  cavity mode.

#### 4.3. Probe RF matching

For reliable RF measurements during the operation of the cavity the RF probe should output a signal value in the range  $(28 \div 32)$  dBm, [19] which corresponds to RF power  $P_p \sim (0.63 \div 1.53)$  W. Details of the RF probe arrangement near the cavity surface are shown schematically in Fig. 10a. The precise adjustment of the RF antenna for the required RF power is a separate step during the cavity RF tuning.

For safety we define the target for the probe output at slightly higher RF power  $P_p = 2$  W. It is a rather small value compared to a pulse RF power of  $P_i \approx 6.3$  MW in operation regime of the cavity. Considering the RF probe as an usual, but strongly mismatched, driving RF coupler and prescribing an external quality factor  $Q_e$ , from S parameters simulations we can estimate the required reflection coefficient  $S_{11}$  and the quality factor  $Q_e$ :

$$Q_e = Q_0 \frac{P_i}{P_p}, \quad S_{11} = \frac{Q_0 - Q_e}{Q_0 + Q_e} = \frac{P_p - P_i}{P_p + P_i} \approx 1 - 2 \frac{P_p}{P_0}, \quad (5)$$

where  $Q_0$  is the own quality factor of the cavity. For a higher precision and sensitivity, simulations in the equivalent sector cavity, see Fig. 5a, were performed and the results were recalculated for the whole gun 5 cavity. An estimated dependence of  $Q_e$  on the insertion  $z_i$  of the antenna tip into the cavity body is plotted in Fig. 10b. The required tip insertion is  $z_i \approx 2.68$  mm. For some mechanical reasons the antenna is tilted with respect to the cavity axis. By moving the RF antenna along the its axis and displacing its tip in the range of  $ds \approx (0.2 \div 0.5)$  mm, we

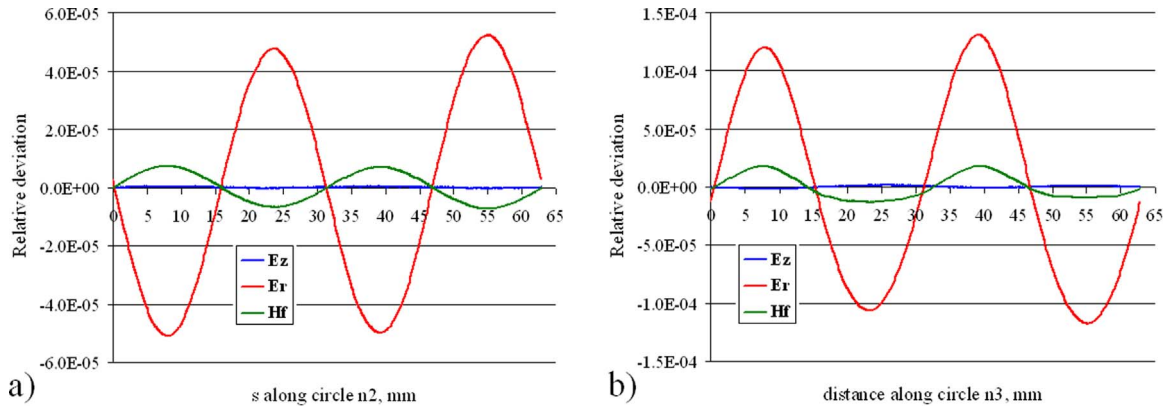


Fig. 9. The plots for relative deviation RD for field components along circle  $n_2$ , (a), and along circle  $n_3$ , (b), see Fig. 8.

expect to get the required RF power at the probe output, see Fig. 10a.

To summarize, the RF probe, implemented in the L-band RF gun cavity, is compatible with the cavity design, does not deteriorate its performance and seems good enough for realization in practice.

### 5. Pulsed RF heating

In the L-band gun cavities the pulsed RF heating effect takes place due to the long RF pulses, [4] and the relatively high peak power. There are two parameters which are significant for describing the effect – the surface temperature rise  $T_{sp}$  and the heat diffusion length  $D_p$  during one RF pulse. Assuming a flat surface, one gets the following equations, [15]:

$$T_{sp} = \frac{2P_d \sqrt{\tau}}{\sqrt{\pi \rho k_c C_p}}, \quad D_p = \sqrt{\frac{k_c \tau}{\rho C_p}} = \sqrt{\alpha_d \tau}, \quad T_{sp} = \frac{2P_d D_p}{\sqrt{\pi} k_c}, \quad (6)$$

where  $\rho$ ,  $k_c$ ,  $C_p$  are material parameters, for OFHC copper they are listed in Table 1. Simulations of temperature rise  $T_{sp}$  and coupled thermal deformations in gun 5 follow the procedure described in [16]. For OFHC copper the thermal diffusivity is  $\alpha_d = 1.135 \times 10^{-4} \frac{m^2}{sec}$  and during the RF pulse length  $\tau = 10^{-3}$  sec the heat penetrates into the cavity body to a depth  $D_p = 336 \mu m$ . The numerically calculated distribution of the surface temperature rise  $T_{sp}$  shown in Fig. 11, coincides with the distribution of the pulsed RF loss density  $P_d$  within an accuracy of the diffusion length  $\sim D_p$ . The maximal calculated surface temperature rise  $T_{sp} = 46.86 \text{ }^\circ C$  agrees well with the estimation given in Eq. (6) where  $T_{sp} = 47.04 \text{ }^\circ C$ .

The pulsed surface heating deformations in the body are proportional to the energy deposited in the body, [17], i.e. displacements of the cavity surface are proportional to time  $0 \leq t \leq \tau$ . Details of the

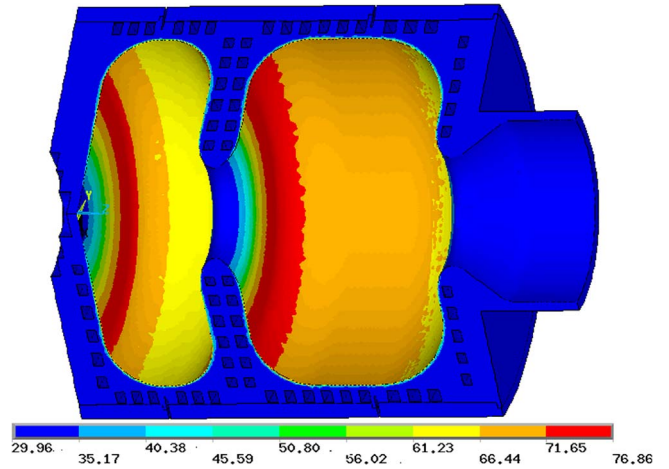


Fig. 11. Calculated distribution of the pulsed temperature rise  $T_{sp}$ , in  $^\circ C$  at the cavity surface.

cavity design are essential for the magnitude of the surface displacements. The frequency shift of the cavity during the RF pulse  $\delta f$  is proportional to the value of surface displacement, i.e. is proportional to time [4]:

$$\delta f = S_t t P_s, \quad 0 \leq t \leq \tau, \quad (7)$$

where the coefficient of proportionality – the cavity sensitivity –  $S_t$ ,  $[\frac{kHz}{MW \cdot ms}]$  is a parameter of the total cavity design.

For the sector of 120 degrees Figs. 12 and 13 show the distributions of the longitudinal and radial deformations due to pulsed heating after the RF pulse with and without stiffening ribs, respectively. The

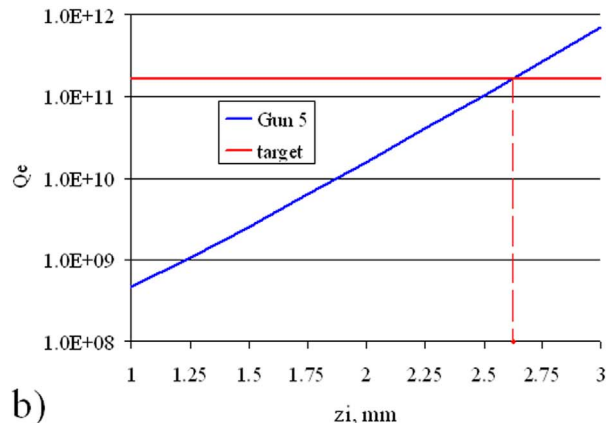
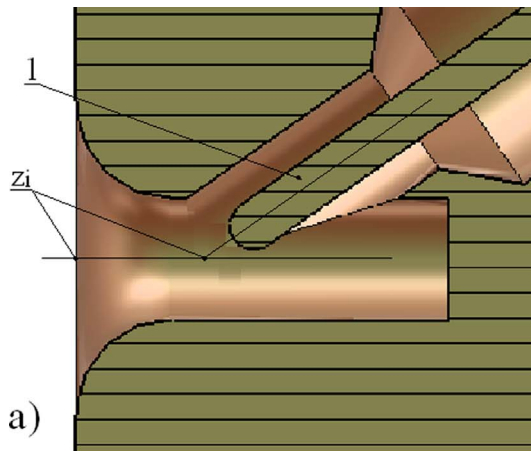


Fig. 10. Sketch of RF probe arrangement (a), 1 - RF antenna, and dependence of external quality factor  $Q_e(z_i)$  on antenna tip insertion  $z_i$  into cavity body, (b).

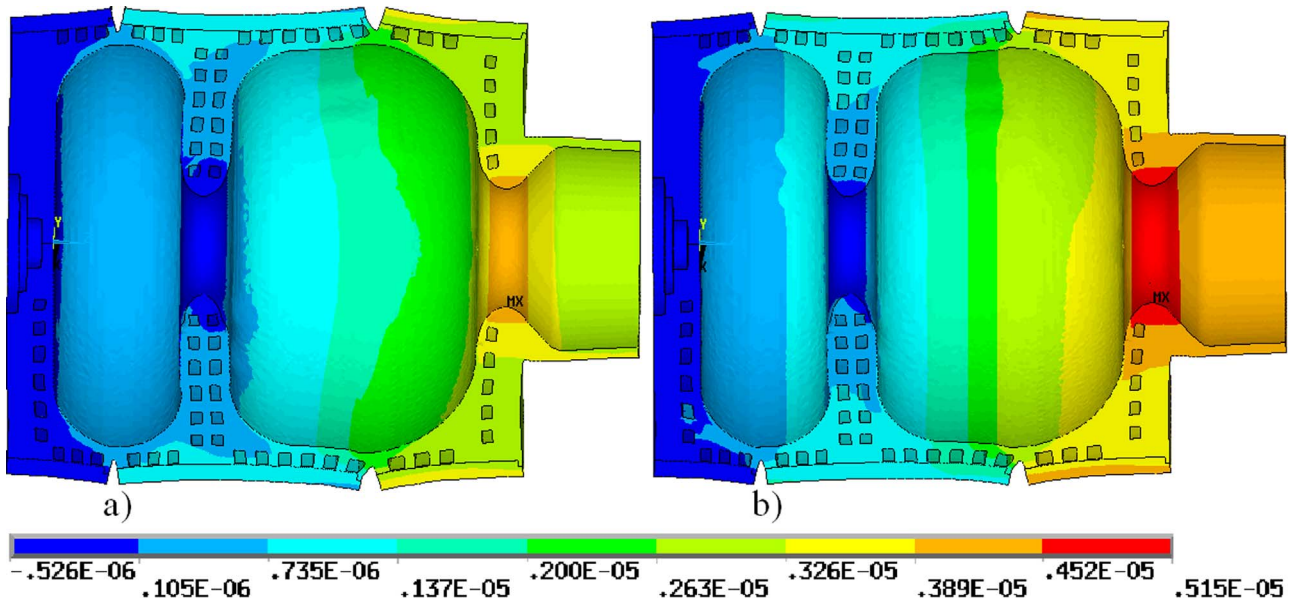


Fig. 12. The distributions of the longitudinal displacements, in m, after the RF pulse in the gun 5 cavity with (a) and without (b) stiffening ribs.

stiffening ribs restrict the cavity expansion both in longitudinal and radial directions, reducing the cavity sensitivity to  $S_l = -2.68 \frac{\text{kHz}}{\text{MW ms}}$  as compared to  $S_l \approx -3.7 \frac{\text{kHz}}{\text{MW ms}}$  for the gun 2 design, [4].

But the ribs introduce a sextupole modulation in the pulsed deformations, which is clearly seen in Fig. 13a. At the cavity RF surface the maximal amplitude of this modulation is  $\approx 1.2 \mu\text{m}$  with a maximal average radial displacement of  $\approx 1.7 \mu\text{m}$  near the brazed joints of the cavity parts. This deviation is less than the tolerances for the cavity manufacturing and non uniform deformations due to average cavity heating. According to Eq. (2), this shape modulation couples operating mode only with sextupole modes. Estimations of the field perturbation by a small sextupole shape modulation were performed in the same way as for the field perturbation by two symmetrical holes for the RF probes. Compared to the quadrupole mode, the sextupole mode in the cavity spectrum is placed at a higher frequency of  $\approx 2700 \text{ MHz}$  and the field components decay faster to the cavity axis. It explains qualitatively results of these special simulations - along circles  $n2$  and  $n3$ , see Fig. 8, we do not see sextupole additions in the field components at the

relative level more than  $2.0 \times 10^{-5}$ .

Gun 5 has practically the same  $Z_h$  value as the reference cavities and practically the same properties for the surface temperature rise  $T_{sp}$  but reduced frequency sensitivity to pulsed deformations.

During pulsed heating a maximal thermal stress  $\sigma$  is induced on the cavity RF surface and, in static approximation, [17,10] can be expressed by:

$$\sigma = \frac{\alpha E_{Ym} T_{sp}}{(1 - \nu)} \tag{8}$$

where  $\alpha$ ,  $E_{Ym}$  and  $\nu$  are material properties, for OFHC copper they are listed in Table 1. This parameter is limiting the tolerable pulse length  $\tau$  for the cavity operation. For a temperature rise above the safe limit where the thermal stress exceeds the elastic limit  $\sigma \geq \sigma_y$  a plastic deformation causing a surface damage appears. For more detailed discussion about tolerable safe limit in  $T_{sp}$  we refer to [10].

Having practically the same  $T_{sp}$  value as the reference cavities, gun 5 has the same properties for the maximal induced thermal stress.

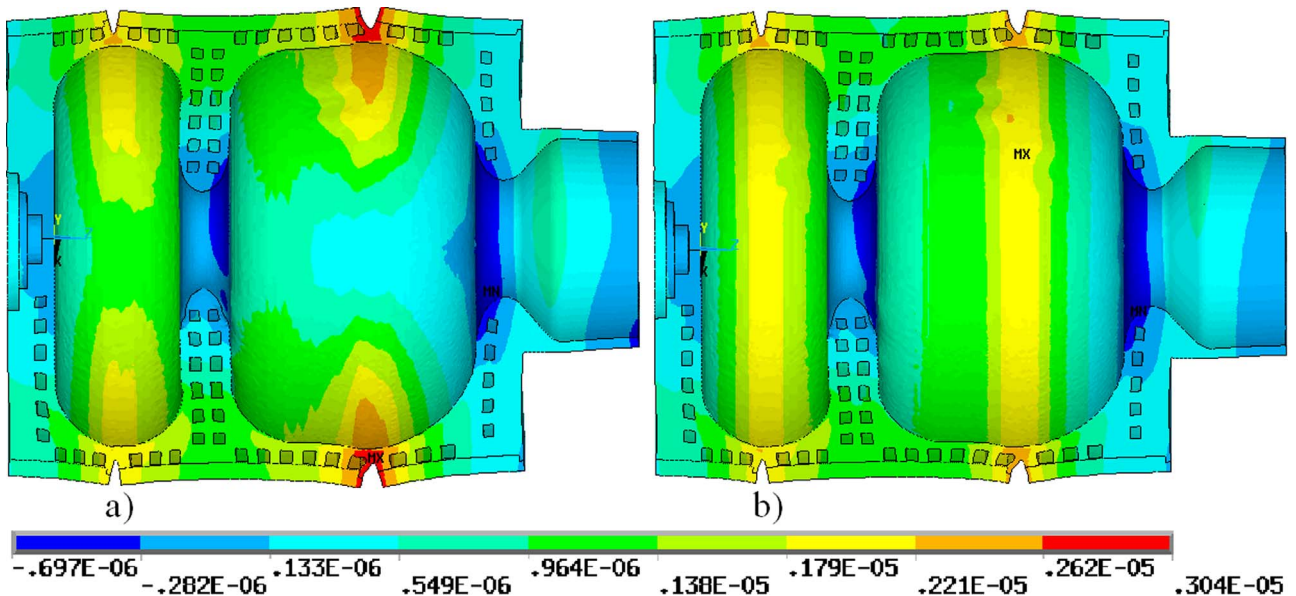
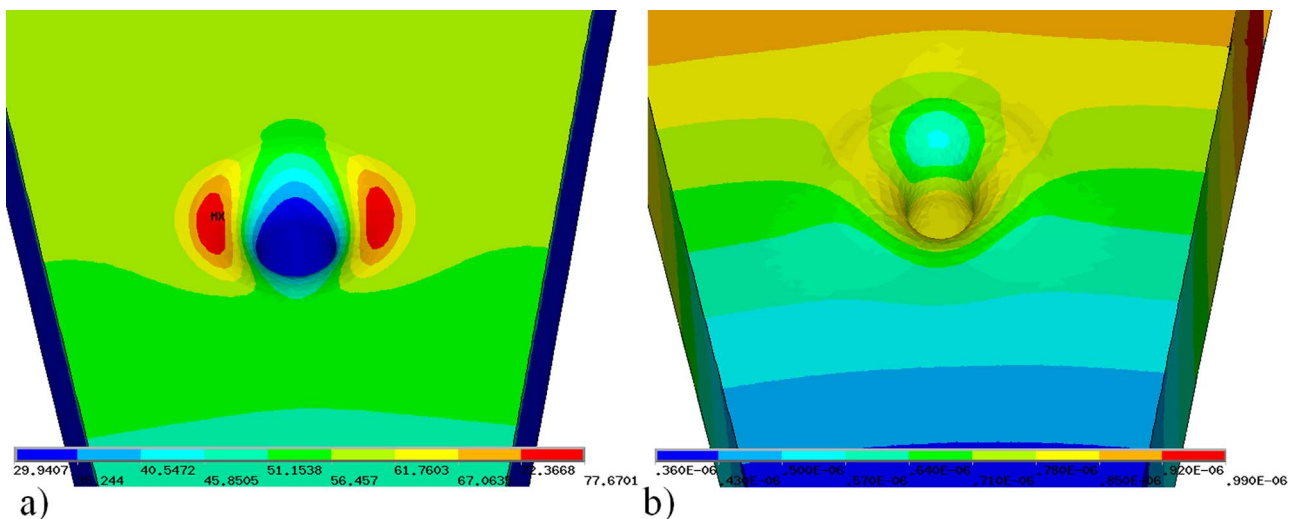


Fig. 13. The distributions of radial displacements, in m, after the RF pulse in the gun 5 cavity with (a) and without (b) stiffening ribs.



**Fig. 14.** The distributions of the temperature rise  $T_{sp}$ , in °C (a), and the total displacements, in m, (b) on the surface in the hole vicinity after the RF pulse.

### 5.1. Pulsed RF heating in the hole vicinity

The local enhancement of the magnetic field in the probe vicinity leads to an increased temperature rise on the surface during the RF pulse. As shown in Fig. 5a, the selected dimensions for the probe hole are rather small compared to the cavity dimensions and the surface shape near the RF probe is rather complicated. The estimation of the surface temperature rise in Eq. (6) is valid for a flat surface, but for the RF probe vicinity it cannot be applied so easily. Direct simulations for RF pulsed heating in the hole vicinity for the equivalent sector cavity were performed assuming values for the magnetic and electric fields in the position of the RF probe, see Fig. 3b.

The distribution of the temperature rise  $T_{sp}$  and the total displacements on the cavity surface in the hole vicinity after the RF pulse are shown in Fig. 14. With the selected dimensions and position of the probe the local enhancement of the magnetic field and the corresponding enhancement in RF loss density are in tolerable limits. The maximal temperature rise in hole vicinity is about  $T_{sp} = 47.6$  °C and does not differ from this value at other cavity parts. The heat diffusion length  $D_p \approx 336$  μm is still smaller than the selected hole dimensions  $r_h$  and  $r_b$ , Fig. 5a. Both,  $T_{sp}$  and stress values are in good agreement with the estimations calculated by Eqs. (6) and (8).

The distribution of the total deformations in the hole vicinity after the RF pulse, shown in Fig. 14b, is rather complicated. The maximal displacement in the hole vicinity with respect to the displacements in the unperturbed cavity is estimated to be about  $\approx 0.12$  μm. Analyzing the  $Q_e(z_i)$  dependence in Fig. 10b, one can see an effect of the change of the probe insertion on the amplitude of the signal from the RF probe. With an increase of the probe insertion  $z_i$  by 1.27 mm  $Q_e$  changes 100 times and field at the antenna tip changes 10 times. A relative change in transformation of the RF signal amplitude from the cavity to the antenna tip is estimated as about 0.1% during the RF pulse. It is a rather small value so not any precision dilution in amplitude measurements is expected. Furthermore, the phase of the signal at the antenna tip does not depend on small changes of the probe insertion.

## 6. Cooling circuit

A cooling circuit of the gun 5 cavity is shown in Fig. 15a. The total circuit consists of ten channels, which can be divided in two groups, different in design.

The first group consists of five channels for cooling the cavity radial walls - the front wall, the iris and the back cathode wall, depicted in Fig. 15b. The second group of five channels serves for the outer cavity cooling, shown in Fig. 15c.

In the cooling circuit design several ideas have been realized.

- Several small channels, distributed in space, are more effective in cooling than one big channel with the same area of cross section. To simplify the connection with the external water circuit and to reduce the number of input/output connectors, the concept of an internal flow distribution is implemented. Thus, the cavity is cooled by 43 small ducts which are fed via ten main channels.
- Due to one turn design used for cooling channels, the dissipated heat can be evacuated rather fast from the cavity.
- The cooling capability of the channels is fitted to the profile of the RF losses in the cavity. The radial channels are developed in a such way as to guide the main portion of the flow with a higher velocity to those parts of the cavity, which have higher RF losses.
- The average flow velocity in the small channels is not more than  $2.0 \frac{m}{s}$ , providing a stable turbulent flow without cavitations. The channels are developed in a such way as to avoid, where possible, whirling, reverse flow in adjacent small channels and other perturbations in the flow uniformity.
- To simplify the water distribution, the pressure drop in all main channels is assumed to be the same.
- To provide a higher flexibility for the connections, all channels are developed symmetrically with respect to their input/output. For the most uniform cooling we assume the opposite flow directions in adjacent channels.

The key point of the cooling circuit is the internal flow distribution and the correct flow arrangement is the critical issue. In turbulent flow the inertial forces strongly dominate over the forces of viscosity of the fluid. Thus, the flow distribution is mainly defined by the motion of the stream. For simulation of the flow distribution with different particularities in the channels, inside ANSYS one can make a choice between several models, leading to slightly different results. To check the flow distribution for the most critical part of the complicated radial cooling channels, special experiments were performed with transparent plastic models, produced by 3D printing, see Fig. 16 on the left. The plastic model precisely contains all the details of the radial channel, critical for the flow distribution. To calibrate the simulations, the experiments were accompanied with appropriate simulations of the flow distribution.

Finally the experiments confirmed the required flow distribution between the channels. In the turbulent regime the flow rate is proportional to the square root of the pressure drop at the channel. The straight lines in the plot in Fig. 16 on the right confirm the linearity of the flow rate in a wide range of pressure drop. And different slopes of

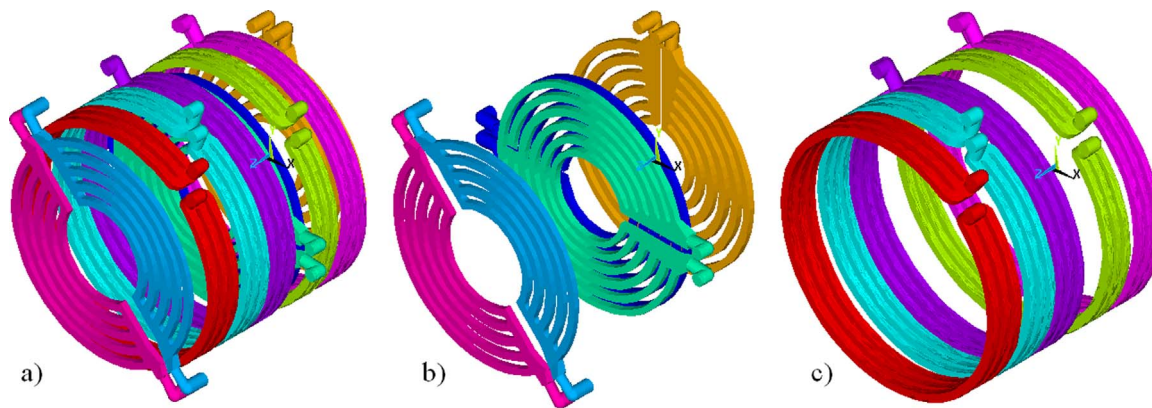


Fig. 15. The total cooling circuit, (a), the group of radial channels (b) and the group of outer channels, (c).

these straight lines confirm the required distribution of the flow between the small channels. The experiments also showed that the channels geometry needs special attention and a high resolution in simulations is required. In the channel design there should be neither sharp obstacles for stream motion nor extra freedom for the stream. Providing extra freedom for the flow we provoke generation of whirling. The flow should be guided softly but distinctly.

We optimized the channels and analyzed technical produceability. All channels can be treated with standard tools. Because the input/output regions in each channel are flow matching regions, the flow optimization for all channels should be performed together with the parts of input/output connectors.

The channels are developed in a such way to avoid, where possible, whirling and extra modulation in the flow velocity distribution.

In Fig. 17 vector distributions of the flow velocity at the input of one radial channel are shown enlarged. As one can see, changing the position of guiding elements in the range of a few millimeters we provide either evident whirling, Fig. 17a, or a smooth flow, Fig. 17b.

The total flow through the channels has to go through their connectors. Therefore, we should use an enlarged internal diameter of the connectors to provide a significant reduction of velocity modulation near connectors. The small channels are close to a square in cross section and the distance between them is comparable with the channel size. This ensures both, an efficient distribution of the flow velocity inside the channel and a large effective surface for heat exchange. The design of the channels for the iris cooling allows the

placement of temperature sensors. For the front wall cooling, two separated half turn channels are developed to keep the general cooling properties and realistic mechanical design for the RF probe avoiding water-vacuum brazed joints.

During operation of the cavity the same pressure drop  $\Delta P_f \approx 35.5$  kPa is foreseen for all channels. The results of simulations and flow distribution test show, see Fig. 16 on the right, a similar flow distribution for the small channels and a stable flow in a wide range of pressure drops between  $0.4\Delta P_f$  and  $3\Delta P_f$ . Furthermore, small deviations of about 0.1 mm in channel dimensions do not lead to essential changes in flow parameters. In adjacent small channels, which belong to the same big channel, the flow has the same direction. Such a scheme is not sensitive to reasonable shortcuts between small channels in the case of inappropriate brazing of cavity parts. For the considered cavity operation regime the expected water consumption is about  $3.3 \frac{m^3}{h}$  for the group of outer channels and about  $4.1 \frac{m^3}{h}$  for the group of radial channels which on the whole add to the total water consumption about  $7.4 \frac{m^3}{h}$ .

### 7. Expected results of the cavity cooling

Investigations of coupled thermo elastic effects in the cavity were following the procedure of coupled simulations presented in [20]. The assumed operating regime corresponds to the average RF power dissipation on the cavity surface  $P_{av} \approx 63.1$  kW, e.g.  $E_c = 60 \frac{MV}{m}$  at the

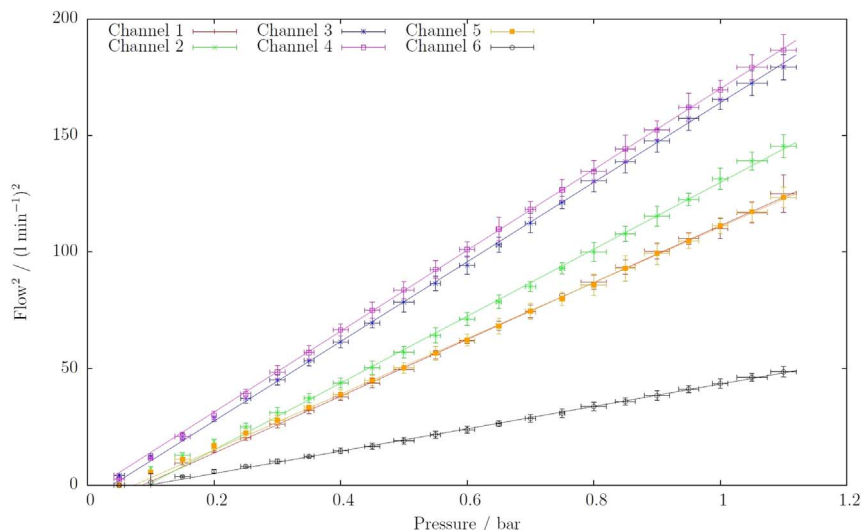


Fig. 16. The transparent plastic model for the test of the flow distribution, on the left, and plots of the flow rate in different channels, on the right.

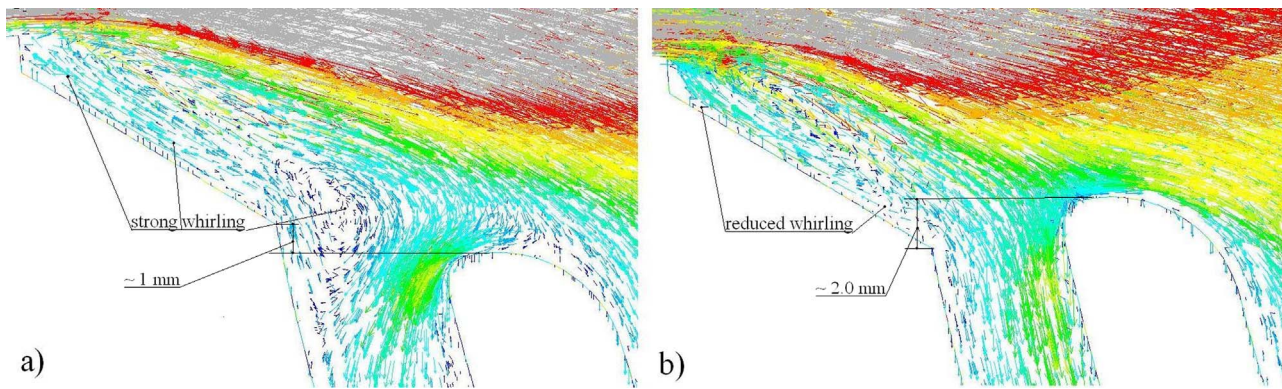


Fig. 17. The vector distribution of flow velocity with a strong whirling (a) and with more uniform flow (b) in the region of flow distribution between small channels.

cathode with an RF pulse length of 1 ms and 10 Hz a repetition rate. Due to a significant rise of the cooling water temperature during its way through the cavity walls, the simulations of the heat exchange with a turbulent flow in the cooling channels were performed with a self consistent approach. Since water parameters, such as density and viscosity depend on the absolute temperature, the input water temperature was assumed to be  $T_{wi}=313\text{ °K}=40\text{ °C}$ .

7.1. Cathode heating

In the complete cavity with a photo cathode the maximal temperature is fixed at the cathode tip. The photo cathode is a special part of the cavity with a cesium telluride  $Cs_2Te$  spot at the tip of the molybdenum plug, Table 1. There is a special holder to connect the cathode to the cavity body, see, for example, [21]. The heat exchange between the cathode and the cavity cannot be described precisely, that's why two extreme approximations – zero heat exchange and perfect exchange – were considered. The back part of the cathode holder was assumed to be at constant room temperature of 300 °K since it is connected to the cathode transfer system. In both extreme cases the cathode tip was the hottest part of the cavity. For zero heat exchange with the cavity body the maximal temperature at the cathode tip was calculated to be  $T=338.6\text{ °K}$ . In this case the heat load on the cathode is only due to RF loss. For a perfect heat contact between the cavity and the cathode plug a temperature distribution in the cavity cross section is illustrated in Fig. 18.

Here the maximal temperature at the cathode tip is about  $\approx 360\text{ °K}$  as the cathode is additionally heated by the cavity. The cathode parts and their related problems are both common for all gun cavities and stay somehow apart from the cooling properties of the cavity itself.

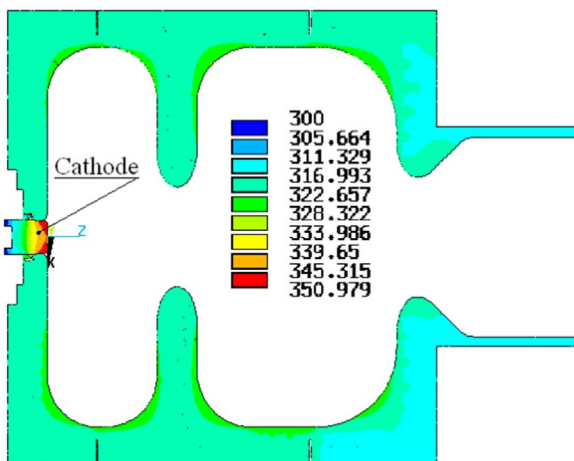


Fig. 18. The distribution of temperatures in the cavity cross section, in °K, assuming a perfect heat contact between the cavity and the cathode.

Compared to the reference design, in the developed cavity the cooling channels are placed closer to the cathode, reducing heating by the cavity.

7.2. Temperature distributions at the cavity without cathode

The water temperature at the input of the cooling circuit is assumed to be 313 °K which therefore is the reference value to estimate the cooling capability of the cavity. With the assumed average RF power dissipation  $P_{av} = 63.1\text{ kW}$  and the pressure drop in the cooling channels  $\Delta P_f \approx 0.35\text{ bar}$  the maximal temperature rise on the inner cavity surface is calculated to be  $\Delta T = 17.67\text{ °K}$ . This scale  $313\text{ °K} \leq T \leq 330.67\text{ °K}$  is for Figs. 19–21.

Temperature distributions in the metal cavity parts (copper body, stainless steel jackets and stiffening ribs) for two perpendicular cross sections are shown in Fig. 19. Due to the deep insertion of the radial channels in the cathode back plane and the irises there is no big temperature increase, it changes in the range from 3°K to 8°K only. This is important since these areas are exposed to strong electric fields. The cooling capability of the channels is fitted to the profile of RF losses, resulting in a rather smooth distribution of the temperature on the inner cavity surface. Temperature distributions on the surface of three cavity parts, see Fig. 2, are shown in Fig. 20. The maximal temperature rise  $\Delta T = 17.67\text{ °K}$  is detected as a hot spot on the cathode wall, Fig. 20a. The cathode wall has the highest total heat load and the hot spot is located near the output of the heated water. At the iris and the front parts the warmed regions with the maximal temperature rise,  $\Delta T = 17.31\text{ °K}$  and  $\Delta T = 15.11\text{ °K}$  respectively, also take place due to both water warming from input to output and a comparatively larger distance between the cooling channels and the cavity surface. Attempts to improve it lead either to deterioration of the RF parameters or to much more complicated design of the cooling channels. The average temperature rise in the vicinity of the RF probe hole on the surface of the front part is in the moderate range  $\Delta T \sim 8.8\text{ °K}$ , Fig. 20c.

The temperature distributions on the surface of the cooling channels are shown in Fig. 21 from two directions. The difference between the output and input water temperatures for all channels, except for the underloaded front radial ones, lies in a narrow range of  $\sim 2\text{ °K}$ . From these distributions one can point out again that the temperature rise in channels along the flow direction is rather uniform, representing a well fitted cooling capability to the profile of RF losses.

Even with a reduced total water consumption, for the same average heat load the developed cavity design and the cooling circuit exhibit temperature rise on the inner cavity surface which is less by half compared to serpentine type channels for radial cooling and multi-turn channels for outer cooling, see, for example, [22], applied for existing cavities.

The total temperature rise on the cavity surface is the sum of the steady state average rise  $\Delta T$  and the temperature rise due to pulsed RF

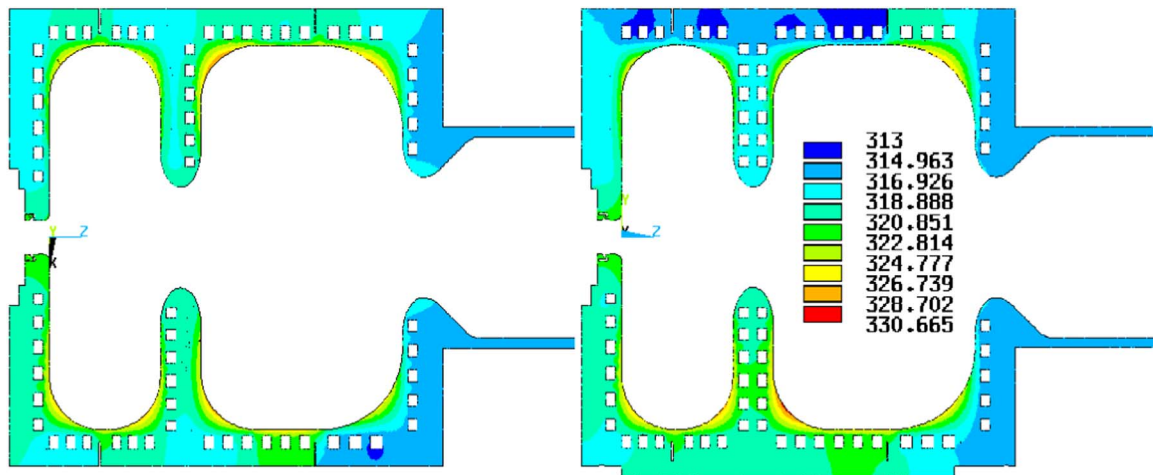


Fig. 19. The temperature distribution in the metal cavity parts for two perpendicular cross sections.

heating  $T_{sp}$ . Having practically the same  $T_{sp}$  value and essentially decreased  $\Delta T$ , the developed cavity will operate with a lower temperature on the surface, as compared to the previous RF gun generations in DESY.

### 7.3. Deformations and internal stress

Due to average heating the cavity expands mainly in longitudinal directions. Distributions of longitudinal displacements in two cavity cross sections are shown in Fig. 22. The total increase of the cavity length is  $\approx 28.2 \mu\text{m}$ . Together with a more uniform expansion of the outer cavity there is a natural bending in the outside direction on the cathode and the front walls. The temperature distributions in Fig. 19 demonstrate that the temperatures on the inner surfaces of these walls are higher than those on the outer surfaces. Hot surfaces expand stronger and provide wall displacements in opposite directions.

The stiffening ribs for average heating are not so important as compared to the displacements due to pulsed RF heating. For the steady state case the temperature of the stiffening ribs is very close to the temperature of the external cavity parts. The coefficients of linear thermal expansion for copper and steel are very similar, see Table 1, and thus the ribs expand similar to the jackets and practically do not provide essential restrictions for longitudinal cavity expansion.

The cavity deformations result in a frequency shift of  $-146.45 \text{ kHz}$ , which is equivalent to a uniform cavity heating at  $7^\circ\text{K}$ . This value is approximately half the maximal temperature rise  $\Delta T \sim 17^\circ\text{K}$ , detected on the cavity surface. This is an another indication that the cooling circuit with an equal pressure drop in all channels provides a uniform cavity cooling in total.

The stress distribution due to average cavity heating doesn't follow

directly the temperature rise on the cavity surface and, in addition, depends on the temperature gradients in the cavity body and its geometry. With stiffening ribs the maximal stress in the total cavity body occurs at the surface of the cavity jacket at the connection between the ribs and the circular parts of the cavity jackets. This value is  $85.5 \text{ MPa}$  which is below the elastic limit of stainless steel.

The stiffening ribs have no essential effect on stress distributions in the copper cavity parts, where the stress is much lower and the calculated maximal value is  $35.4 \text{ MPa}$ , which is approximately less by half than the accepted yield stress  $62 \text{ MPa}$ , see Table 1. The distributions of the von Mises stress on the inner cavity surface are shown in Fig. 23 for different parts of the cavity on a common scale – the maximal value is equal to  $35.4 \text{ MPa}$ . From the simulations one can conclude that on the inner cavity surface the stress values are below  $23.6 \text{ MPa}$ , except some region on the cathode wall. Such moderate values are the result of reduced temperature gradients in the cavity body due to a more uniform cooling.

Between  $24 \text{ MPa}$  and  $35.4 \text{ MPa}$  stress values take place on the surface of the cooling channels and near the brazed surfaces. It can be reduced by slightly rounded shapes of the cross sections of the channels which however will complicate the design.

The analysis shows a significant reserve in the average dissipated power for gun 5. Considering elastic deformation, defined by the yield stress, as a limiting factor for the cavity, we regard the dissipated power up to  $P_{av} \approx 110 \text{ kW}$  as tolerable.

### 8. Cavity rigidity and modes of acoustic oscillations

Due to small transverse dimensions of the cooling channels the cavity has a low frequency sensitivity to deviations of the average water

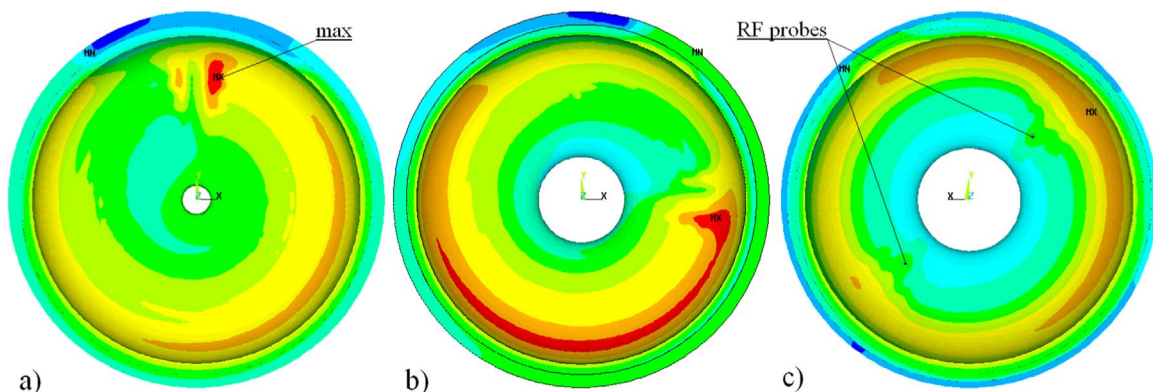


Fig. 20. The temperature distributions on the surface of the three cavity parts: cathode part (a), iris part (b), front part (c).

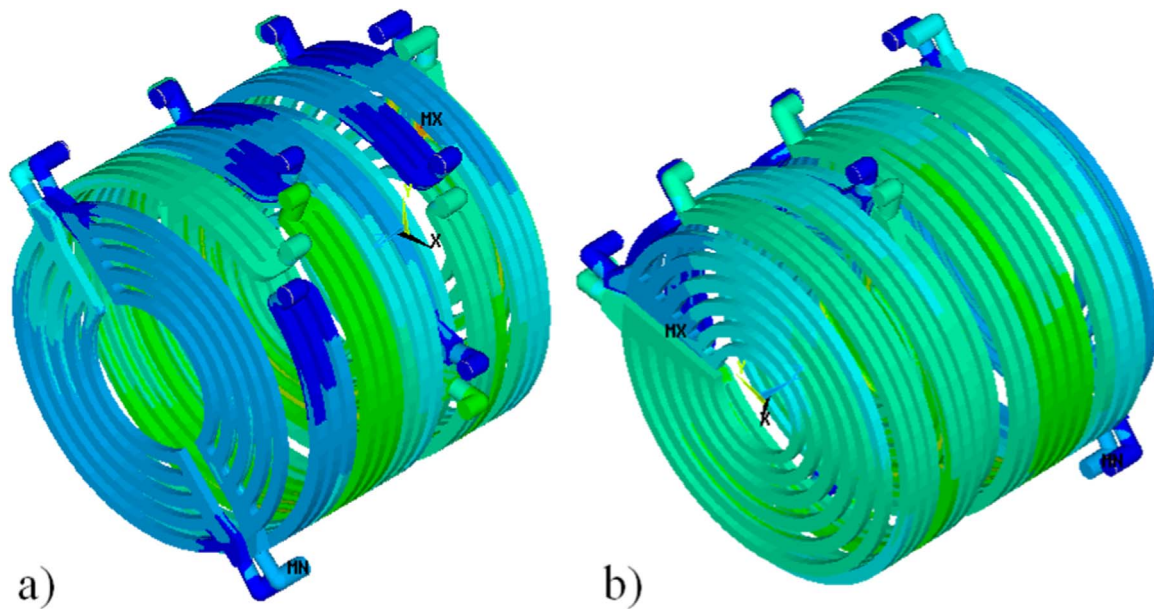


Fig. 21. The temperature distributions on the surface of cooling channels for two points of view: from the cavity front (a), and from the cathode wall (b).

pressure in the cooling channels. For a pressure variation of 1 bar the displacements on the cavity surface are calculated to be less than 0.1 μm, providing a tiny frequency sensitivity of about  $-42 \frac{\text{Hz}}{\text{bar}}$ .

The ambient pressure after vacuum pumping of the cavity results in stronger bending of the walls inside the cavity which is estimated as about 2 μm. These deformations lead to a positive frequency shift of about 910 Hz.

The developed cavity design is more rigid, compared to the existing cavities, and less sensitive to external perturbations. This improves the stability of operation. After manufacturing, the cavity should be tuned precisely to operating frequency and suitable field balance in cells. The established current procedure of cavity tuning is based on plastic deformations of the front and, if required, the cathode walls. With increased thickness of these walls, the longitudinal force required for the same frequency shift of the cavity cells, is twice as much as that of for gun 4.

The modes of acoustic oscillations in the cavity, estimated with the standard ANSYS procedure, start above ≈600 Hz. For lower acoustic modes details of the cavity connection and mounting are significant. For several modes in the frequency range from 600 Hz to 2800 Hz the whole cavity oscillates with very small mutual displacements of cavity elements. Hence, such modes of oscillations will cause only minor

perturbations in the cavity frequency.

The modes with significant mutual displacements inside the cavity start with frequencies  $f \geq 2800$  Hz. Fig. 24 illustrates the distribution of total displacements on the outer cavity surface and inside the cavity for the acoustic mode with the frequency  $f=3100$  Hz. It is a membrane-like oscillation of the radial cavity parts which can, depending on the amplitude of excitation, result in a frequency shift of the operating RF mode. However, such acoustic modes always occur in RF gun cavities due to priorities to other parameters in cavity optimization. In the developed cavity design such acoustic modes at least do not appear at lower frequencies than for other optimized designs and are far above frequencies of typical pulsations, e.g. ~50 Hz.

### 9. Summary

A summary of the expected parameters for the gun 5 cavity reference design is presented in Table 2. They are opposed to the same calculated parameters of the existing gun 4 [6]. The relative values in the column “Relation” are calculated with respect to the parameters for gun 4.

The design of gun 5 realizes a set of counterbalanced, optimized and mutually fitted solutions.

Due to its optimized RF shape gun 5 has a higher quality factor,

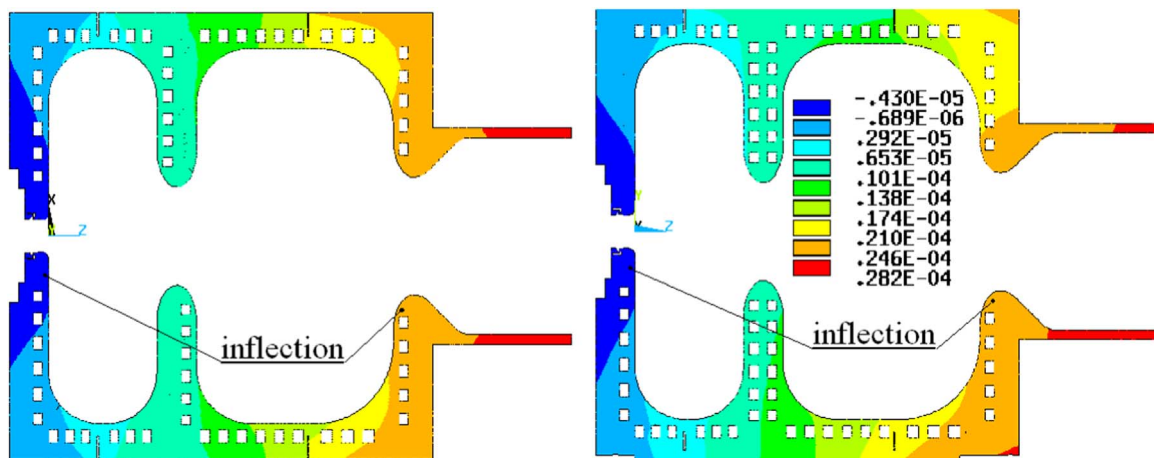


Fig. 22. The distribution of longitudinal displacements, in m, in the metal cavity parts for two perpendicular cross sections.

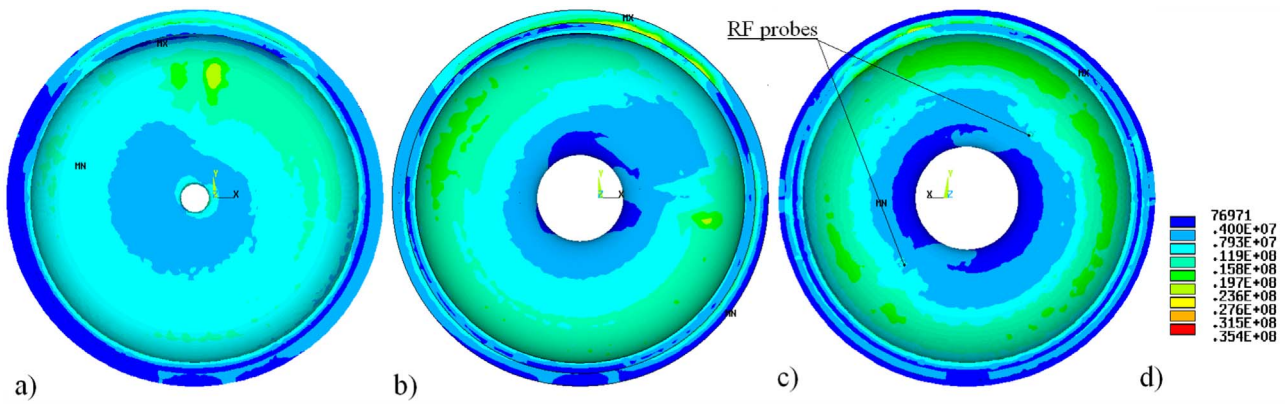


Fig. 23. The distributions of von Miss stress, Pa, on the surface of cavity parts: cathode part (a), iris part (b), front part (c).

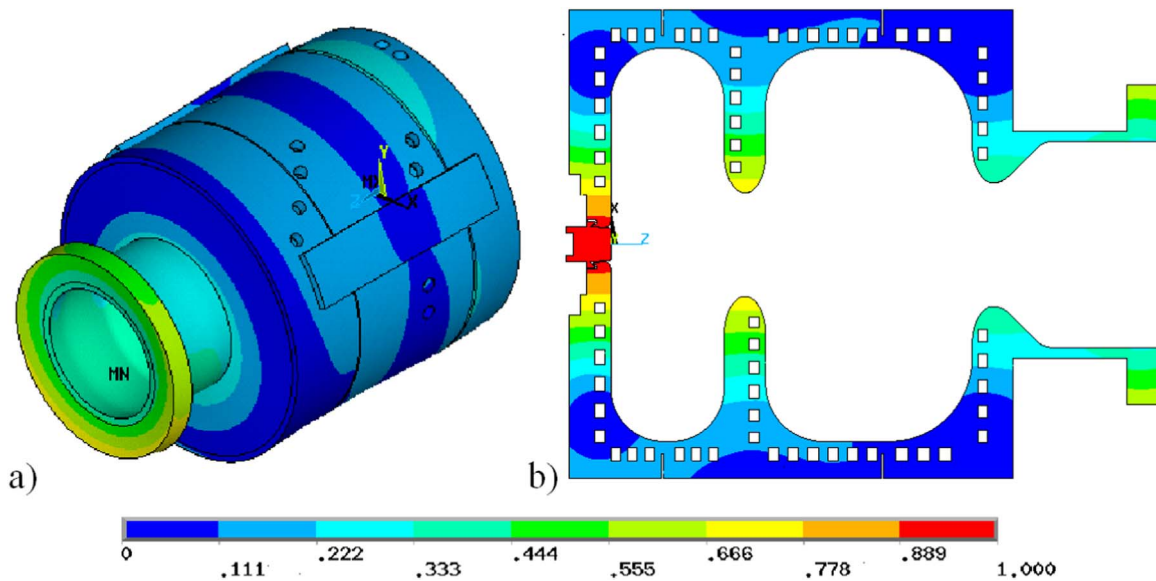


Fig. 24. The distribution of total displacements, relative units, for the acoustic mode with frequency  $f=3100$  Hz, at the outer cavity surface (a), and in cavity cross section, (b).

Table 2  
Summary of the expected parameters for the gun 5 cavity.

Parameter	Unit	gun 5	gun 4	Relation
Cathode RF field	MV	60	60	=
Surface RF field	$\frac{\text{m}}{\text{MV}}$	60.6	72	<15.8%
Quality factor		25770	23400	>10.1%
Pulse RF power	MW	6.31	6.43	<1.8%
Modes separation	MHz	6.07	5.07	>19.7%
RF probes		Yes	No	
Pulsed surf. temp. rise <sup>a</sup>	°C	46.86	45.2	>3.7%
Pulsed deformation <sup>a</sup>	μm	4.59	9.3	<50.6%
Frequency shift <sup>a</sup>	kHz	-16.89	-17.36	<2.7%
Average RF power <sup>b</sup>	kW	63.1	64.3	<1.8%
Aver. surf. temp. rise, max. <sup>b,c</sup>	°C	17.67	32.5	<45.6%
Frequency shift <sup>b,c</sup>	kHz	-146	-226	<35.4%
Power sensitivity <sup>b,c</sup>	$\frac{\text{kHz}}{\text{kW}}$	-2.31	-3.52	<34.4%
Number of water I/O		10	14	
Water consumption <sup>c</sup>	$\frac{\text{m}^3}{\text{h}}$	7.44	10.5	<29.1%

<sup>a</sup> With RF probe vicinity, after  $\tau=1$  ms RF pulse.

<sup>b</sup> For 1% Duty Factor (DF) operation.

<sup>c</sup> For an average flow velocity of  $2.0 \frac{\text{m}}{\text{s}}$  in the independent channels of gun 4 and a pressure drop 0.353 bar in all channels of gun 5.

needs less RF pulse power to provide the required electric field at the cathode, has a significantly reduced electric field at the cavity iris and the improved separation in frequency to the 0 mode. All this will improve the reliability and parameters stability during cavity operation.

Furthermore, the full cavity cell is equipped with an RF probe, intended to measure the RF field phase and amplitude directly from the cavity. The probe position and its dimensions are selected and optimized in a set of contradictory limitations. The found solution can be realized without deteriorating other cavity parameters.

Due to pulsed RF heating gun 5 is similar to the existing gun cavities in the maximal temperature rise on the surface. But the expected maximal value of the total temperature rise due to both, pulsed RF heating and dissipated average RF power, is fewer  $\sim 14$  °C. This will improve reliability of operation and the cavity parameters stability. The improved rigidity of the cavity results in a smaller frequency shift during one RF pulse.

Comparing further parameters, such as possibility of multipacting, spectrum of own acoustic modes etc., we can say that the proposed cavity design is at least not worse than the existing L-band gun cavities.

Due to its elaborated and optimized cooling circuit, with the reduced consumptions of cooling water, gun 5 shows a strongly reduced temperature rise on the inner cavity surface, hence a reduced frequency shift and besides the maximal internal stress stays well within the elastic limit for OFHC copper. This definitely will improve the stability of the cavity parameters in operation with a duty factor of

~1%.

The proposed gun 5 cavity design seems more suitable for operation with the present specification in unique facilities, [1,2] and has a significant reserve for upgrades in the average dissipated RF power.

In the declared total list of parameters the newly developed gun 5 cavity exceeds the existing DESY gun cavities of previous generations and the L-band cavities known from other references, [22,23].

### Acknowledgements

The authors thank a lot of colleagues, especially K. Floettmann, V. Fogel, J. Sekutowicz, S. Lederer, M. Bousonville from DESY in Hamburg, A. Oppelt, M. Krassilnikov, J. Meissner, J. Schulze, J. Hoffmann from DESY in Zeuthen, D. Richter from Helmholtz Zentrum in Berlin and N. Brusova, A. Feschenko, Yu. Kalinin, L. Kravchuk from INR for their help, support, useful and critical comments during this development.

### References

- [1] M. Altarelli, et al., European XFEL Technical Design Report, DESY, Hamburg, Germany, Rep. DESY 2006-097, DESY-European XFEL, 2007.
- [2] M. Vogt, et al., The Free-Electron Laser FLASH at DESY, in: Proceedings IPAC'13, Shanghai, China, May 2013, pp. 1167–1169.
- [3] S. Komamiya, International Linear Collider, Latest Status Towards Realization, in: Proceedings IPAC'16, Busan, Korea, May 2016, pp. 1–5.
- [4] V. Paramonov, et al., Pulsed RF Heating Particularities in Normal-conducting L-band Cavities, in: Proceedings Linac'2006, Knoxville, USA, 2006, pp. 646–648.
- [5] B. Dwersteg, et al., RF gun design for the TESLA VUV Free Electron Laser, NIMA 393 (1997) 93–95.
- [6] S. Rimjaem, et al., Tuning and Conditioning of a New High Gradient Gun Cavity at PITZ, in: Proceedings EPAC'08, Genoa, Italy, 2008, pp. 244–246.
- [7] ANSYS, (<http://www.ansys.com>).
- [8] MWS (<http://www.cst.com>).
- [9] J.W. McKenzie, et al., Cavity design for S-band Photoinjector RF gun with 400 Hz Repetition Rate, in: Proceedings IPAC'14, Dresden, Germany, June 2014, pp. 2983–2985.
- [10] D. Pritzkau, R. Siemann, Experimental study of rf pulsed heating on oxygen free electronic copper, Phys. Rev. ST Accel. Beams 5 (2002) 112002.
- [11] V. Paramonov, et al., RF Gun Development with Improved Parameters, in: Proceedings Linac'08, Vancouver, Canada, September 2008, pp. 627–629.
- [12] K. Floettmann, ASTRA – A space charge tracking algorithm, (<http://www.desy.de/~mpyflo>).
- [13] G. Romanov, Simulation of Multipacting in HINS Accelerating Structures with CST Particle Studio, in: Proceedings Linac'08, Vancouver, Canada, September 2008, pp. 166–168.
- [14] V. Baglin, et al., The Secondary Electron Yield of Technical Materials and its Variation with Surface Treatment, in: Proceedings EPAC'2000, Vienna, Austria, 2000, pp. 217–221.
- [15] P.B. Wilson, Scaling linear colliders to 5 TeV and above, in: ITP Conference on Future High Energy Colliders, Univ. of California, Santa Barbara, CA, USA, 1996.
- [16] V. Paramonov, A. Skasyrskaya, Pulsed RF heating simulations in normal conducting L-band cavities, DESY, Hamburg, Rep. TESLA-FEL 2007-04, 2007.
- [17] A.D. Kovalenko, Introduction to thermoelasticity, Kiev, USSR, Naukova dumka, 1965.
- [18] V. Kulman, Accelerating system, in: B. Murin (Ed.), Ion Linear Accelerated 2, Atomizdat, Moscow, USSR, 1978, pp. 36–46.
- [19] L. Jachmann, Private communications.
- [20] S. Joshi, et al., The Complete 3-D Coupled RF-Thermal-Structural-RF Analysis Procedure for A Normal Conducting Accelerating Structure for High Intensity Hadron Linac, in: Proceedings Linac'2002, Gyeongju, Korea, 2002, pp. 216–218.
- [21] M. Otevel, et al., Report on Gun Conditioning Activities at PITZ 2013, in: Proceedings IPAC'14, Dresden, Germany, June 2014, pp. 2962–2964.
- [22] J.H. Han, H. Huang, Numerical Study of the RF Heating of an L-band Gun, in: Proceedings PAC'09, Vancouver, Canada, May 2009, pp. 627–629.
- [23] F. Marhauser, et al., A high Average Power RF Photoinjector Gun Cavity Developed for the BESSY Soft X-Ray FEL, in: Proceedings FEL'06, Dresden, Germany, August 2006, pp. 560–562.